

We are IntechOpen, the world's leading publisher of Open Access books Built by scientists, for scientists

6,900

Open access books available

186,000

International authors and editors

200M

Downloads

Our authors are among the

154

Countries delivered to

TOP 1%

most cited scientists

12.2%

Contributors from top 500 universities



WEB OF SCIENCE™

Selection of our books indexed in the Book Citation Index
in Web of Science™ Core Collection (BKCI)

Interested in publishing with us?
Contact book.department@intechopen.com

Numbers displayed above are based on latest data collected.
For more information visit www.intechopen.com



Standard Calculation of Fault Current Contribution of Doubly Fed Induction Generator-Based Wind Turbine

Ahmed El-Naggar

Additional information is available at the end of the chapter

<http://dx.doi.org/10.5772/63450>

Abstract

The fault current contribution of the doubly fed induction generator-based wind turbines (DFIG-WTs) is dictated by a combination of factors, including the electrical parameters of the machine and the controller configuration of the converters. A detailed manufacturer-based simulation model for DFIG-WT was used for detailed analysis of the controller influences on short-circuit parameters. Based on the analysis, new approximate expressions of the short-circuit parameters were introduced and a new mathematical model of the short-circuit current were developed. The mathematical models and the expressions were later validated using nonlinear optimization for parameter extraction. Subsequently, a new method was introduced for fault current contribution calculation in a simple and reliable way similar to IEC-60909. The method is based on linearization and a newly introduced correction factor that takes the influence of the controller into account. Finally, the new introduced method was tested on a small wind farm and the results show better accuracy in comparison with IEC-60909.

Keywords: DFIG-WT, short-circuit, transient impedance, fault, time constant

1. Introduction

Until 1998, the majority of the installed wind turbines were of fixed speed type [1]. It is a cheap and simple technology but with many inherent disadvantages. Yet, these never created any unmanageable difficulties until the introduction of grid codes. The wind turbine technology has since developed rapidly in order to match the stipulated requirements as well as to optimize energy yields, efficiency, and overall costs. The commercial wind turbine concepts can generally be classified into fixed speed, limited variable speed, and variable-speed turbines. Variable-

speed wind turbines can also be classified based on the location of the converter as partial or full-scale power electronic converter. Whether a turbine uses geared drive or direct-drive can be used as further criterion for classification [1, 2].

Currently, the doubly fed induction generator-based wind turbine (DFIG-WT) is the dominating concept [3]. In this setup, a DFIG is used as shown in **Figure 1**, where the stator is directly connected to the grid and the rotor is linked through a partially rated power electronic converter to enable variable-speed operation. The dynamic speed range is dependent on the size of the frequency converter. A typical rating for the latter is 25–30% of the generator capacity leading to a typical speed range of $\pm 30\%$ around the synchronous speed [2]. The frequency converter also allows for the slip power to be fed into the. Moreover, it allows for reactive power compensation and smooth grid connection. The multistage gearbox as well as the slip rings is still inevitable to have some drawbacks, such as heat dissipation from friction, increase need for maintenance and audible noise.

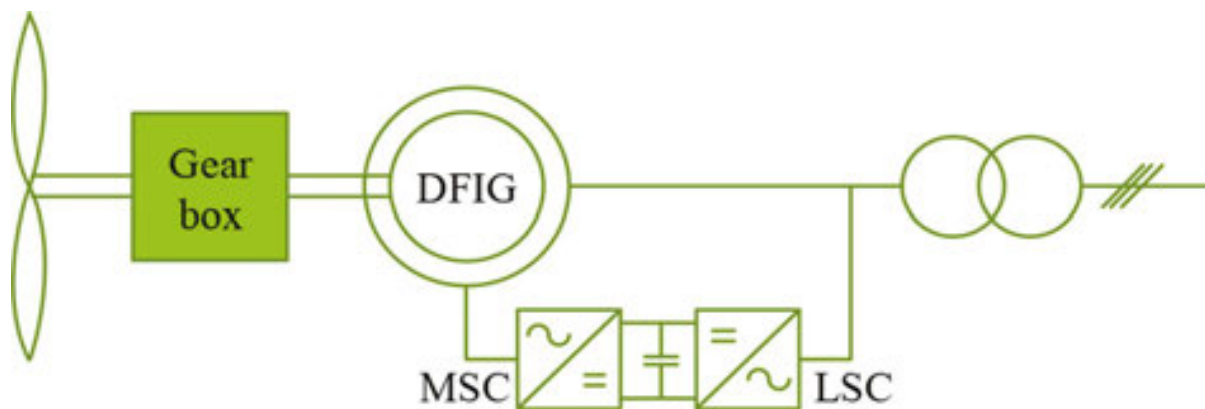


Figure 1. Layout of variable-speed DFIG-WT.

2. Modeling of DFIG-WT

The role of the DFIG is to convert the mechanical power captured by the rotor blade from the wind into electrical power, while the voltage source converter (VSC) generates the required rotor and DC voltages in relation to the control signals.

2.1. Modelling of VSC circuit

Power electronics converters are used for power flow control in variable-speed drives during steady state and dynamic periods. In DFIG-WT, the back-to-back low voltage two-level converter shown in **Figure 2** is commonly used owing to its simplicity [4]. Additionally, it allows for power generation in sub- and super-synchronous mode, active and reactive power control, and harmonic compensation [5].

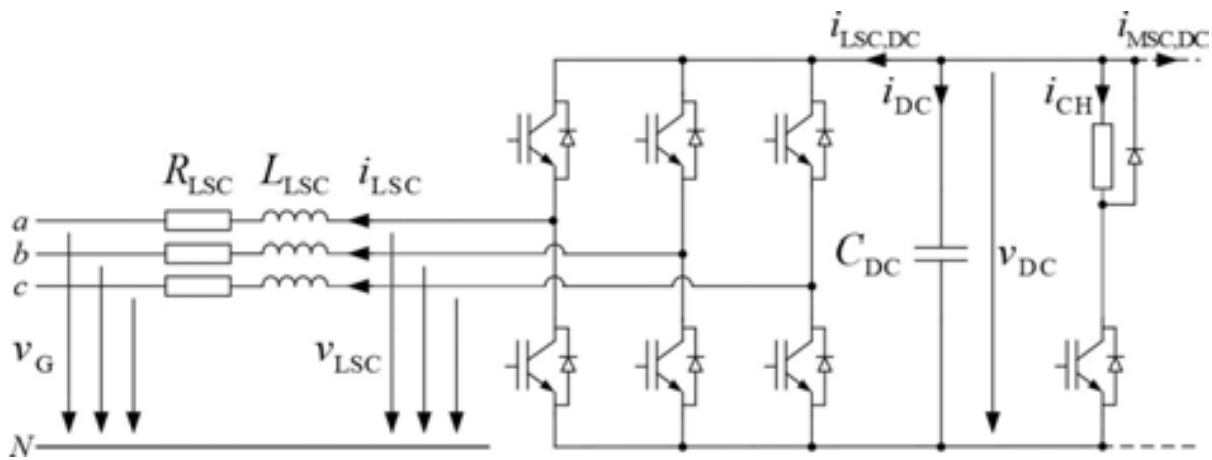


Figure 2. Two-level voltage source converter.

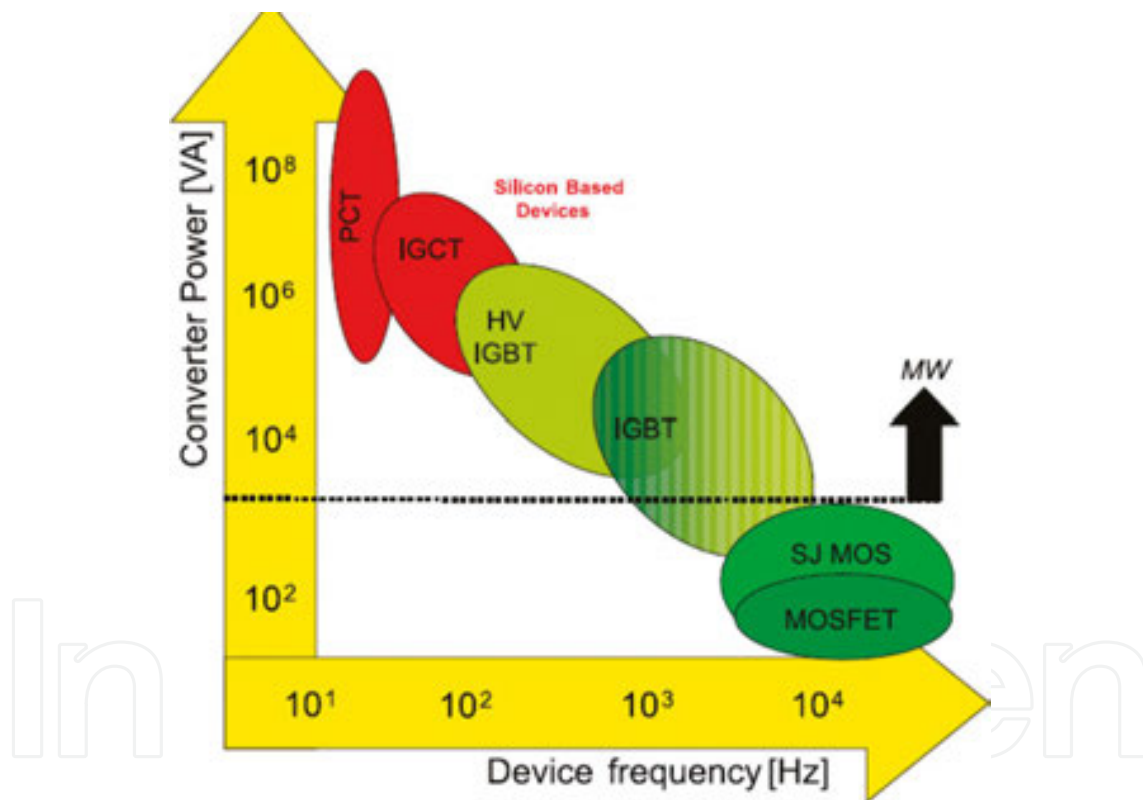


Figure 3. Switching frequency ranges of semiconductor devices [7].

The IGBT is the dominating semiconductor device used in converter systems for DFIG-WT. It offers turn-on and turn-off capability; thus, allowing full controllability over a wide range of switching frequencies. The switching frequency is determined by the switching losses, which limits the upper limit to approximately 5 kHz, and the harmonic generation, which limits the lower limit to approximately 500 Hz as depicted in **Figure 3**. The IGBT is a combination of a bipolar junction transistor (BJT) and MOSFET placed monolithically on the same silicon wafer

to combine the qualities of both devices [6]. Therefore, the IGBT can be modeled as a BJT driven by a MOSFET, where the IGBT properties are influenced by the parasitic elements of the IGBT structure as shown in the equivalent circuit of **Figure 4**. The physical interpretation and designations of the parasitic elements of the IGBT equivalent circuit are evident in [7].

The switching process of the IGBT is very fast, which requires very small simulation time steps (0.1–1 ns) to achieve high accuracy in the results. Such small simulation time steps will result in high-computational effort for the simulation of a full wind turbine system, correspondingly more for wind farms. An alternative method to increase the simulation time step and reduce the computational effort is to replace the semiconductor devices by ideal switches. The implementation of ideal switches allows the investigation of harmonics generation and interactions with the filter circuits.

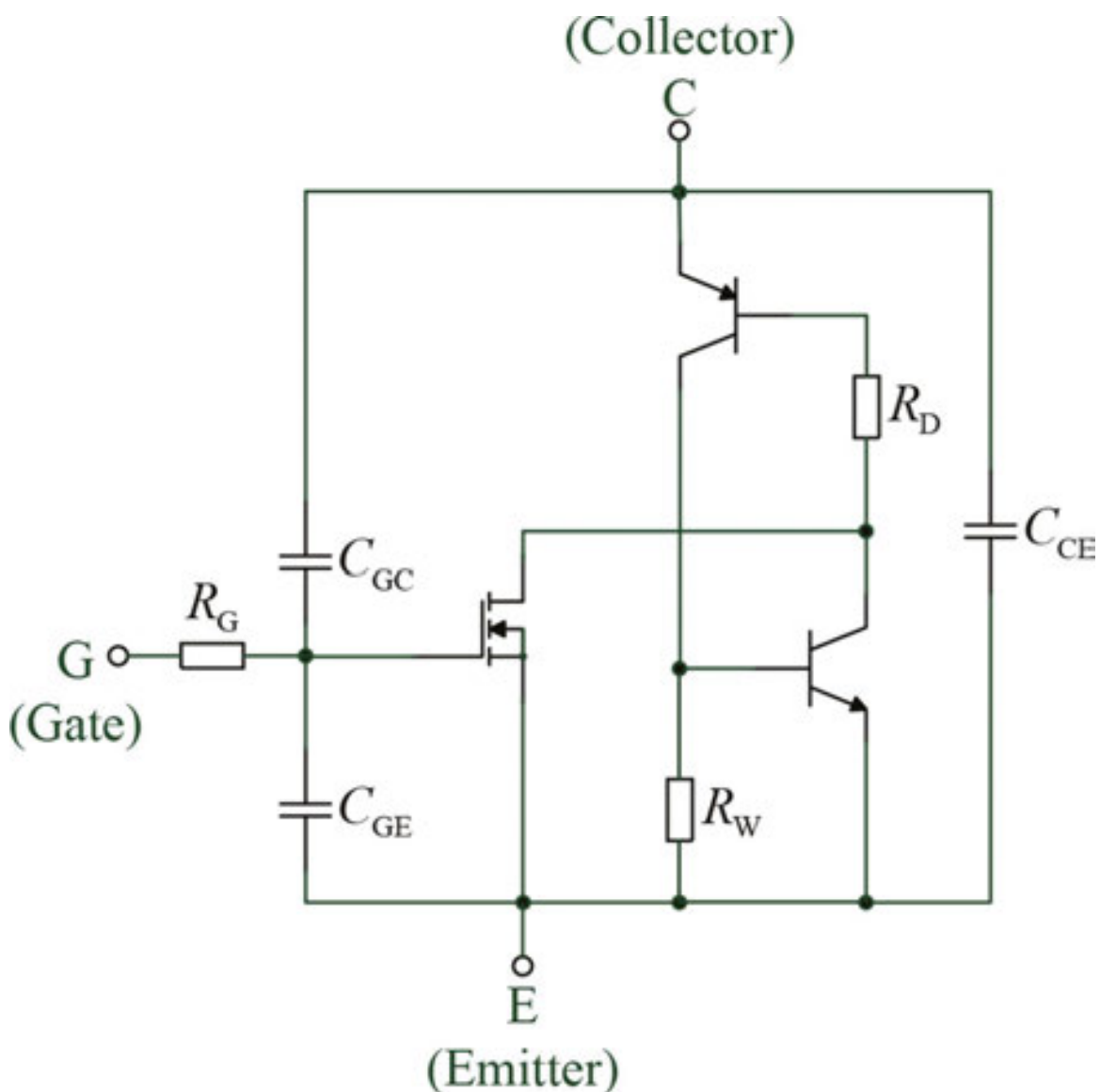


Figure 4. Equivalent circuit diagram of IGBT.

2.2. DC circuit

The DC circuit as shown in **Figure 2** consists of a DC capacitor and braking chopper. The DC capacitor is used to suppress the interfering voltages originating from the rectification process and to prevent fast and large oscillations in the DC voltages, while the braking chopper is used to protect the IGBT against high DC bus voltages that may occur during fault conditions. The value of DC capacitor is chosen based on the time constant required to charge the capacitor from zero to the rated voltage if supplied by the nominal power. This time constant is given by the following:

$$\tau = \frac{1}{2} \frac{C_{DC} V_{DC,N}^2}{S_N} \quad (1)$$

where $V_{DC,N}$ is the nominal DC voltage and S_N is the wind turbine nominal power.

It should be noted that from now on, all the relations will be expressed in per unit quantities expressed by small character rather than capital one as in Eq. (1).

The DC capacitor time constant is usually set between 5 and 10 ms to satisfy low ripple and overvoltage in the DC voltage and to allow for fast active and reactive power.

The differential equation describing the DC voltage neglecting the losses is given by the following:

$$\frac{dv_{DC}}{dt} = \frac{1}{c_{DC}} \cdot i_{DC} = \frac{1}{c_{DC}} (-i_{LSC,DC} - i_{MSC,DC} - i_{CH}) = \frac{1}{c_{DC} \cdot v_{DC}} (-p_{LSC} - p_{MSC} - p_{CH}) \quad (2)$$

where

$$p_{CH} = \begin{cases} 0 & , \text{ if chopper off} \\ \frac{v_{DC}^2}{r_{CH}} & , \text{ if chopper on} \end{cases} \quad (3)$$

2.3. Generator

The voltage equation of the DFIG using machine variables shown in **Figure 5**, assuming identical stator and rotor windings, and uniformly distributed three phase windings whose axes displaced 120 may be expressed as follows:

$$\begin{bmatrix} v_{S,abc} \\ v_{R,abc} \end{bmatrix} = - \begin{bmatrix} r_{S,abc} & 0 \\ 0 & r_{R,abc} \end{bmatrix} \begin{bmatrix} i_{S,abc} \\ i_{R,abc} \end{bmatrix} - \frac{d}{dt} \begin{bmatrix} \psi_{S,abc} \\ \psi_{R,abc} \end{bmatrix} \quad (4)$$

The flux linkages maybe expressed for magnetically linear system as follows:

$$\begin{bmatrix} \psi_{S,abc} \\ \psi_{R,abc} \end{bmatrix} = \begin{bmatrix} l_{S,abc} & l_{M,abc} \\ l_{M,abc} & l_{R,abc} \end{bmatrix} \begin{bmatrix} i_{S,abc} \\ i_{R,abc} \end{bmatrix} \tag{5}$$

All the relations stated in Eqs. (4) and (5) are in p.u. quantities, where all the parameters and variables are normalized on the machine rated power and voltage as a base. Additionally, all the rotor variables are referred to the stator windings using the stator-rotor turns ratio. The assumption that the machine operating point remains in the linear range and the windings are identical is a simplification that is not satisfied for all type of studies. However, it is adequate for behavior prediction in most applications [8].

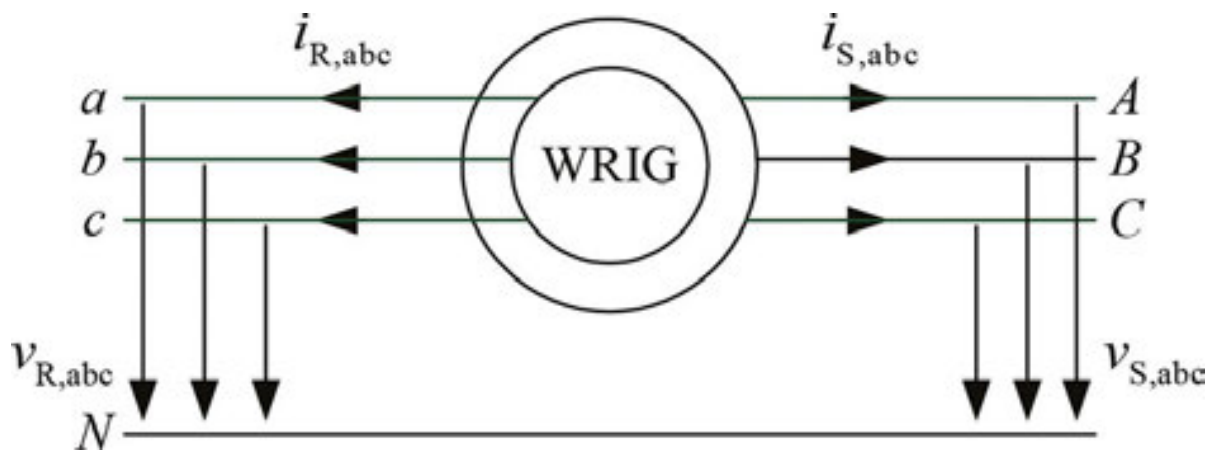


Figure 5. Doubly fed induction generator with measured quantities.

It is usually desirable to express the machine variables as a space vector with arbitrarily chosen reference frame. The space vector model of the DFIG in a fixed reference frame is as follows:

Voltage equations:

$$\begin{aligned} \underline{v}_S^{\angle 0} &= -r_S \underline{i}_S^{\angle 0} - s \underline{\psi}_S^{\angle 0} \\ \underline{v}_R^{\angle 0} &= -r_R \underline{i}_R^{\angle 0} - (s - j\omega_r) \underline{\psi}_R^{\angle 0} \end{aligned} \tag{6}$$

Flux equations:

$$\begin{aligned} \underline{\psi}_S^{\angle 0} &= l_S \underline{i}_S^{\angle 0} + l_M \underline{i}_R^{\angle 0} \\ \underline{\psi}_R^{\angle 0} &= l_R \underline{i}_R^{\angle 0} + l_M \underline{i}_S^{\angle 0} \end{aligned} \tag{7}$$

Electromagnetic torque:

$$t_{el} = \text{Im}\{\underline{\psi}_s \cdot \underline{i}_s^*\} = \text{Im}\{\underline{\psi}_R \cdot \underline{i}_R^*\} \quad (8)$$

Equation of motion:

$$2H_R \frac{d\omega_R}{dt} = T_{Aero} - T_{El} \quad (9)$$

Eqs. (6)–(9) constitute the full-order model (FOM) of the DFIG used for dynamic simulations.

The analysis of the transient response as well as control of the DFIG requires the transfer function of the DFIG currents, which can be derived from FOM after some mathematical manipulation as follows:

Stator current:

$$\begin{aligned} \underline{i}_s^{\angle 0} &= \frac{-(r_R + (s - j\omega_R)l_R)l_M \underline{v}_s^{\angle 0} + s l_M^2 \underline{v}_R^{\angle 0}}{s^2 \sigma l_S l_R + s(l_R r_S + l_S r_R - j\omega_R \sigma l_S l_R) + r_S(r_R - j\omega_R l_R)} \\ &= \underline{G}_{SZ} \underline{v}_s^{\angle 0} + \underline{G}_{SW} \underline{v}_R^{\angle 0} \end{aligned} \quad (10)$$

Rotor current:

$$\begin{aligned} \underline{i}_R^{\angle 0} &= \frac{(s - j\omega_R)l_R l_M \underline{v}_s^{\angle 0} - (r_S + s l_S)l_R \underline{v}_R^{\angle 0}}{s^2 \sigma l_S l_R + s(l_R r_S + l_S r_R - j\omega_R \sigma l_S l_R) + r_S(r_R - j\omega_R l_R)} \\ &= \underline{G}_{RZ} \underline{v}_s^{\angle 0} + \underline{G}_{RW} \underline{v}_R^{\angle 0} \end{aligned} \quad (11)$$

where $\sigma = 1 - \frac{l_M^2}{l_S l_R}$ is the leakage coefficient.

The frequency response of stator and rotor currents to stator and rotor voltages is shown in **Figures 6** and **7**, respectively. In the low frequency range (0–1 Hz), the frequency response to stator voltage has high magnitude, while the response to the rotor voltage shows negative magnitudes. This is because in the low frequency range (setting the Laplace operator to zero) the rotor circuit is seen from the stator side as closed circuit and the stator impedance becomes purely resistive, while the rotor impedance becomes infinite as seen from the rotor. On the other hand, in the frequency range around the rotor speed (setting the Laplace operator to $j\omega_R = j1.2\omega_0$), the phenomena is reversed, where the rotor is seen from the stator side as an open circuit, while the rotor impedance becomes purely resistive as seen from the rotor.

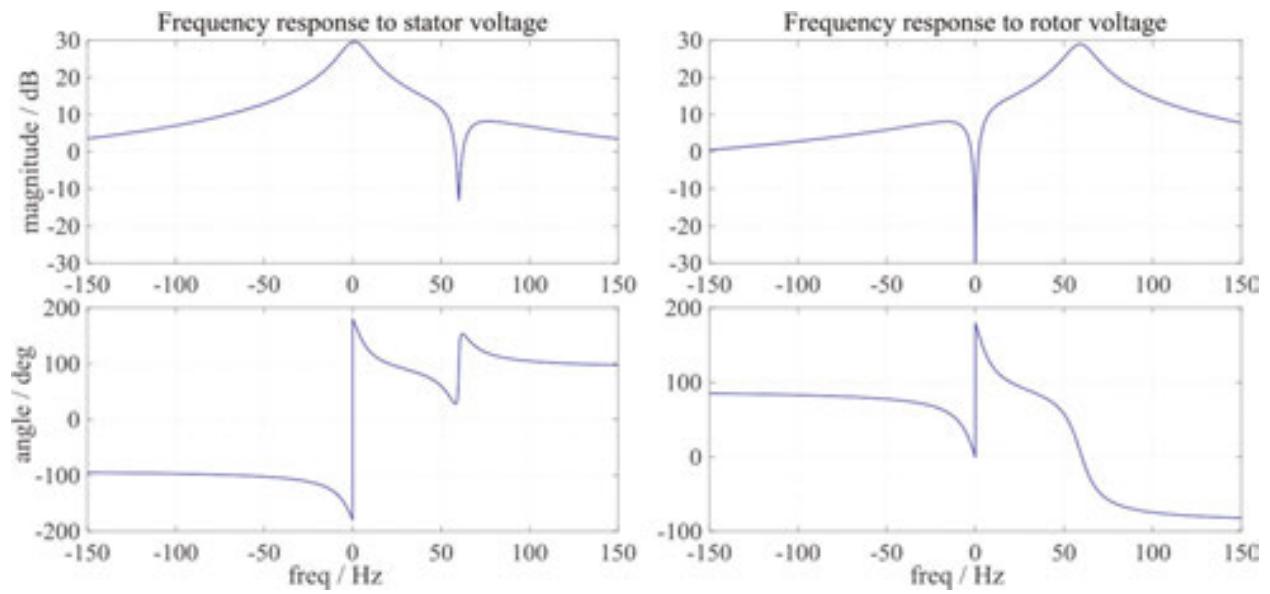


Figure 6. DF IG stator frequency response.

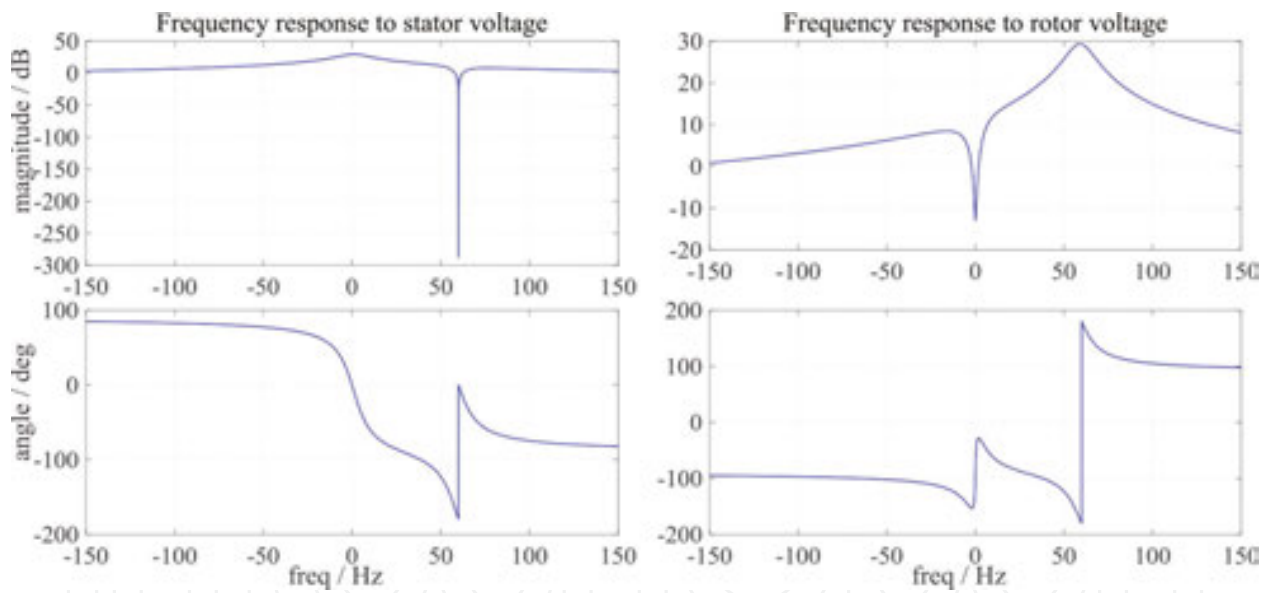


Figure 7. DF IG rotor frequency response.

3. Fault current contribution analysis

Knowledge of fault current contribution of the wind power plants is crucial for power system design and protection system setting. According to analyses in various studies [9–12], it was assumed that the fault current contribution of the DF IG-WT is dictated only by its electrical parameters. Yet, this would be true if only the crowbar protection circuit was engaged directly

upon fault occurrence. However, the crowbar operation is no longer desired due to the long deactivation period which leads to loss of controllability and incompatibility with the currently applicable fault ride through specific requirements. Under such configuration when no crowbar exists and full controllability is still in place, the fault current contribution of the DFIG-WT is dictated by a combination of factors, including the electrical parameters of the machine and the controller configuration of the converters [13].

The fault current contribution of the DFIG is the sum of both the machine and the line side converter (LSC) contributions. Usually, the DFIG contribution dominates, but it will be shown later that the response of the LSC is too fast and the reactive current capability of the LSC is utilized for grid voltage support during faults [13]. Therefore, the LSC contribution cannot be ignored. The fault response of the DFIG-WT will be separately analyzed for both the DFIG and LSC, starting from their natural responses till their responses with the full controller.

3.1. LSC natural fault response

Assuming a linear inductor and neglecting the switching behavior of the converter, the voltage equation of the LSC, based on the configuration of **Figure 2**, in fixed reference frame is given by the following:

$$v_{LSC}^{\angle 0} = v_G^{\angle 0} + (r_{LSC} + s l_{LSC}) i_{LSC}^{\angle 0} \quad (12)$$

Rearranging Eq. (12) yields the transfer function of the LSC current as follows:

$$i_{LSC}^{\angle 0} = \frac{v_{LSC}^{\angle 0} - v_G^{\angle 0}}{r_{LSC} + s l_{LSC}} = G_{LSC}(s) \cdot (v_{LSC}^{\angle 0} - v_G^{\angle 0}) \quad (13)$$

Solving the Eq. (13) for a step change in the grid voltage yields:

$$i_{LSC}^{\angle 0}(t) = \frac{\Delta v_{LSC}^{\angle 0} - \Delta v_G^{\angle 0}}{r_{LSC} + j\omega_0 l_{LSC}} e^{-\frac{r_{LSC}}{l_{LSC}} t} + i_{LSC,ss}^{\angle 0} \quad (14)$$

According to Eq. (14), the fault response of the LSC current is similar to the natural response of an RL-circuit, with a steady state fault current $i_{LSC,ss}^{\angle 0}$ and a DC decaying current of a magnitude dependent on the change of grid and LSC voltages and a time constant determined by the choke parameters.

3.2. LSC fault response with feed-forward control

The LSC voltage as well as the steady state current is dependent on the controller configuration and the internal set-points. Therefore, a proper analysis of the LSC fault response requires the converter control equation to be plugged into Eq. (13).

The current control loop of the LSC converter is based on a feed-forward term and a PI-controller to compensate for measurement uncertainties. The feed-forward term is found by replacing the Laplace operator in the transfer function by the operating frequency. Accordingly, the resulting controller becomes

$$\underline{v}_{LSC}^{\angle v_G} = \left(k_p + \frac{k_i}{s} \right) \left(\underline{i}_{LSC,ref}^{\angle v_G} - \underline{i}_{LSC}^{\angle v_G} \right) + \underline{v}_G^{\angle v_G} + \underline{z}_{LSC} \underline{i}_{LSC}^{\angle v_G} \tag{15}$$

Figure 8 shows the resulting inner current control loop considering the input measurement delays and the converter dead time. The transfer function of the input measurement filter and the PWM converter dead time as a PT1 delay element and a first-order Padé approximation is, respectively, as follows:

$$G_{meas}(s) = \frac{1 + j\omega_0\tau_{meas}}{1 + \tau_{meas}s} \tag{16}$$

$$G_{dt}(s) = \frac{-s(2\tau_{dt} + j\omega_0) + 2j\omega_0\tau_{dt} + 4\tau_{dt}^2}{s(2\tau_{dt} - j\omega_0) - 2j\omega_0\tau_{dt} + 4\tau_{dt}^2}$$

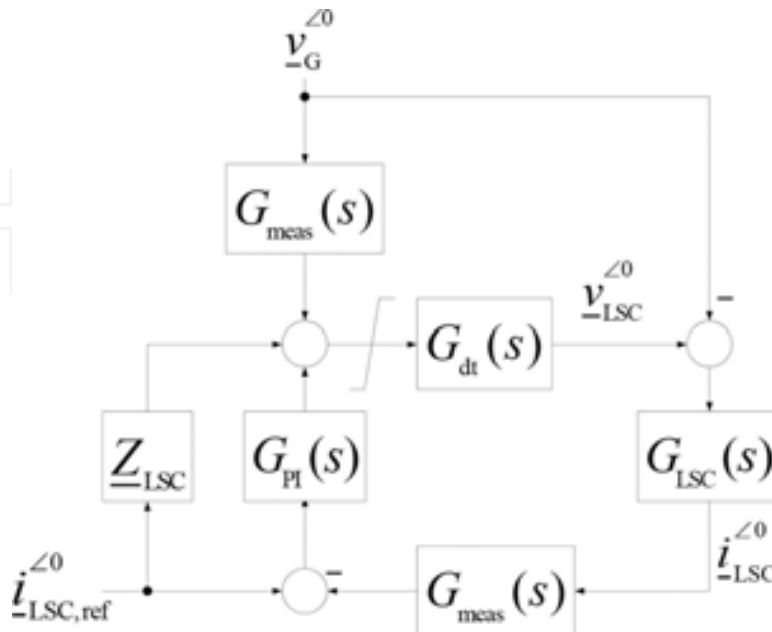


Figure 8. LSC converter inner current control loop.

The closed-loop transfer function of the LSC current according to **Figure 8** is given by the following:

$$i_{LSC}^{\angle 0} = \frac{G_{dt}(s) \cdot (G_{pl}(s) + z_{LSC}) i_{LSC,ref}^{\angle 0} + (G_{dt}(s) \cdot G_{meas}(s) - 1) v_G^{\angle 0}}{1 + G_{LSC}^{-1}(s) + G_{dt}(s) \cdot G_{meas}(s) \cdot G_{pl}(s)} \quad (17)$$

The characteristic polynomial of Eq. (17) is of fifth order, which can be solved in radicals, only if the sixth-degree resolvent possesses a rational solution (Galois Theory) [14]. Solving the quartic function as given in [15, 16] would result in highly complex formula. However, if both $G_{meas}(s)$ and $G_{dt}(s)$ are neglected, considering that their time constants are in order of few hundreds of μs , the transfer function would be reduced to a quadratic function given by the following:

$$i_{LSC}^{\angle 0} = \frac{(s - j\omega_0) \left(\frac{1}{\tau_{kp}} + j\omega_0 \right) + \frac{1}{\tau_{ki}}}{s^2 + s \left(\frac{1}{\tau_{kp}} - j\omega_0 \right) + \frac{1}{\tau_{ki}} - j \frac{\omega_0}{\tau_{kp}}} i_{LSC,ref}^{\angle 0} \quad (18)$$

where $\tau_{kp} = \frac{l_{LSC}}{r_{LSC} + k_p}$, $\tau_{ki} = \frac{l_{LSC}}{k_i}$ and $k_I = \frac{k_p}{\tau_i}$.

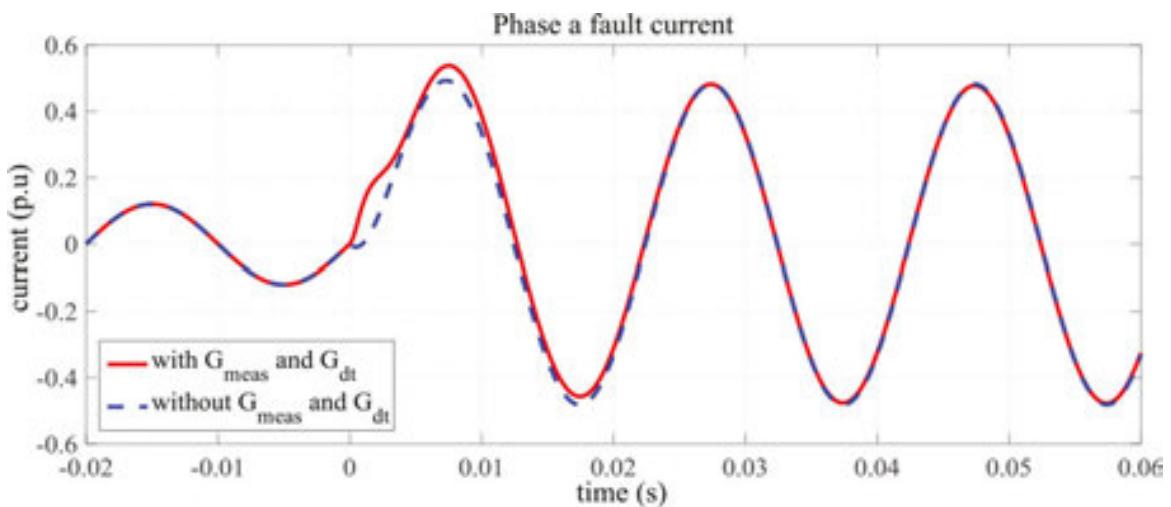


Figure 9. Influence of measurement and dead-time delays on LSC short-circuit current.

Figure 9 illustrates the small influence of neglecting $G_{meas}(s)$ and $G_{dt}(s)$ on the short-circuit current of the LSC. This simplification resulted in a full rejection of the disturbance quantity $\Delta v_G^{\angle 0}$, and the resultant response would only be dictated by the change in the reference tracking quantity $\Delta i_{LSC,ref}^{\angle 0}$ which will result in two transient currents that decay with time constants

and frequencies that can be found by solving the general quadratic formula [17] of the characteristic polynomial in Eq. (18) as follows:

$$\begin{aligned} \frac{1}{\tau_{DC}} + j\omega_{DC} &= -\frac{1}{2\tau_{kp}} + j\frac{\omega_0}{2} - \sqrt{\left(\frac{1}{2\tau_{kp}} + j\frac{\omega_0}{2}\right)^2 - \frac{1}{\tau_{ki}}} \\ \frac{1}{\tau_{AC}} + j\omega_{AC} &= -\frac{1}{2\tau_{kp}} + j\frac{\omega_0}{2} + \sqrt{\left(\frac{1}{2\tau_{kp}} + j\frac{\omega_0}{2}\right)^2 - \frac{1}{\tau_{ki}}} \end{aligned} \quad (19)$$

According to Eq. (19), the time constants and frequencies are dependent on the line choke and the PI-controller parameters. The later are usually tuned to result in over-damped response, which means that one of the two transient currents decreases much faster than the other with a time constant nearly equal to τ_{kp} and negligible frequency, while the other has a dynamic coefficient that approaches zero. Consequently, both transient currents can be ignored and it can be considered that the output current tracks the reference current directly without any dynamics. This is evident in **Figure 10**, which shows the tracking behavior of the output current. Therefore, it could be concluded that the LSC behaves as a current source with the reference current as a set-point.

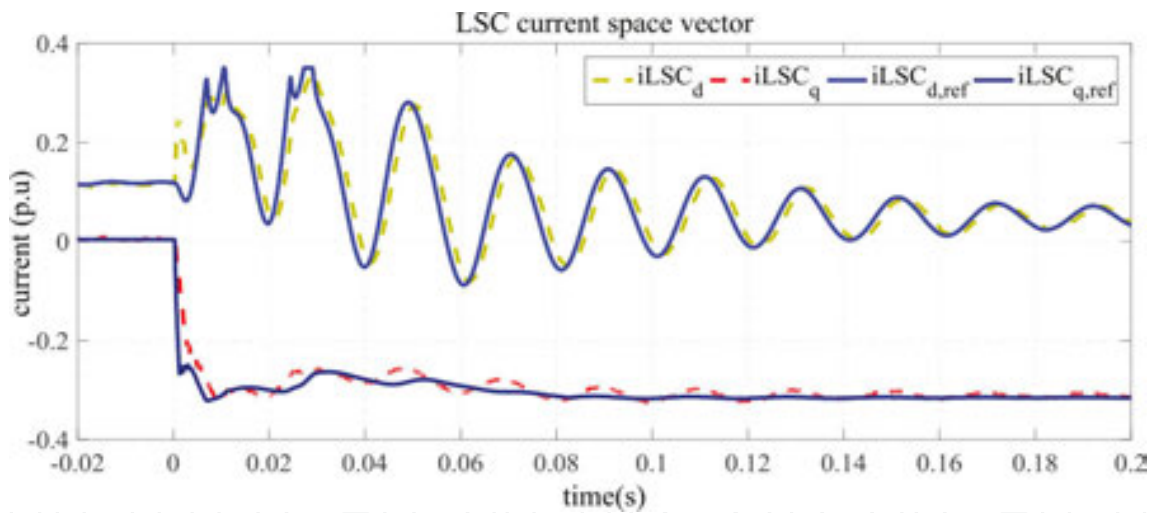


Figure 10. LSC short-circuit current space vector.

3.3. DFIG natural fault response

The characteristic polynomials in Eqs. (10) and (11) are identical and of second order. This implies that the short-circuit current of the stator and rotor will contain two decaying transient currents and that decay with the same time constants and Eigen frequencies but with different magnitudes for the stator and rotor. Those time constants and Eigen frequencies are found by solving the general quadratic formula in the same manner as in Eq. (19). However, that would result in complex formulas as given in [13]. An alternative method is to use the singular

perturbation to separate the fast and slow dynamics from one another, which yields the following expressions:

$$\frac{1}{\tau_{DC}} - j\omega_{DC} \approx \frac{r_s(r_r - j\omega_r l_r)}{l_s(r_r - j\omega_r \sigma l_r)}, \quad \frac{1}{\tau_{AC}} - j\omega_{AC} \approx \frac{r_r(r_s + j\omega_0 l_s)}{l_r(r_s + j\omega_0 \sigma l_s)} - j\omega_r$$

$$\underline{z}'_{-S1} \approx r_s + j\omega_0 l_s \frac{(r_r - j\omega_r \sigma l_r)}{(r_r - j\omega_r l_r)}, \quad \underline{z}'_{-R1} \approx r_r + j(\omega_0 - \omega_r) l_r \frac{(r_s + j\omega_0 \sigma l_s)}{(r_s + j\omega_0 l_s)}$$
(20)

Finally, the natural fault current response of the DFIG can be expressed as follows:

$$i_{-S1}^{\angle 0}(t) \approx i_{-S1,ss}^{\angle 0} - \frac{\Delta v_{-S1}^{\angle 0}}{\underline{z}'_{-S1}} e^{-\left(\frac{1}{\tau_{DC}} - j\omega_{DC}\right)t} + \frac{j\omega_0 l_M \Delta v_{-R1}^{\angle 0} - r_r \left(\frac{1}{\sigma} - 1\right) \Delta v_{-S1}^{\angle 0}}{\underline{z}'_{-R1}} e^{-\left(\frac{1}{\tau_{AC}} - j\omega_{AC}\right)t}$$
(21)

Figure 11 shows the resultant transient and steady state currents of DFIG natural fault response.

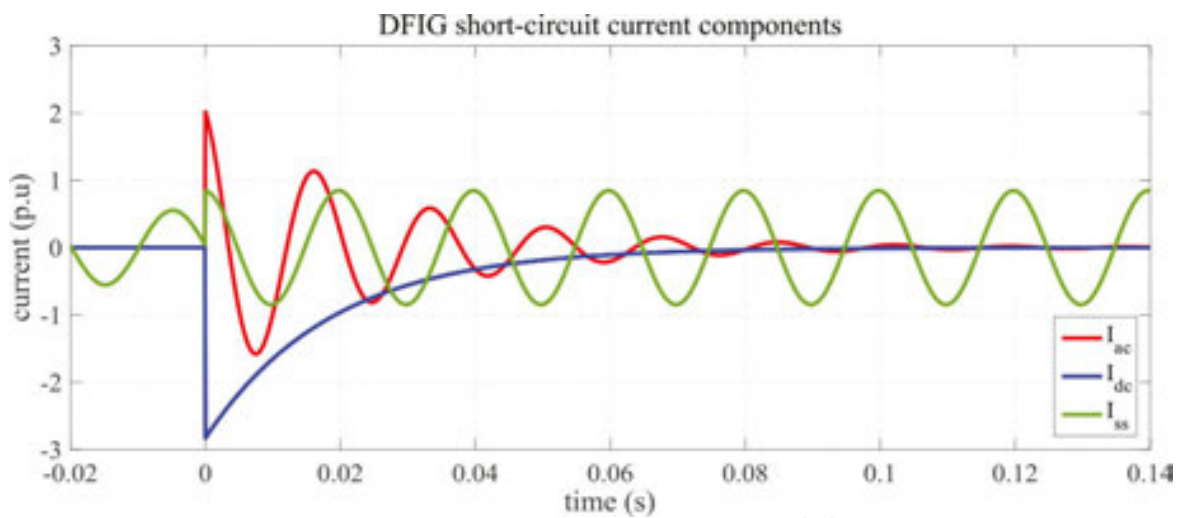


Figure 11. DFIG natural short-circuit current components.

3.4. DFIG fault response with feed-forward control

The DFIG closed-loop controller has the same structure as the LSC, where the current control loop is dependent on a feed-forward term derived from rotor voltage equation and a PI-controller to compensate for steady state errors. Accordingly, the resultant controller becomes

$$\begin{aligned} \underline{v}_R^{\angle v_s} &= -(r_R + js_G \omega_0 \sigma l_R) \underline{i}_R^{\angle v_s} + s_G \frac{l_M}{l_S} \underline{v}_S^{\angle v_s} - \left(k_p + \frac{k_I}{s} \right) (\underline{i}_{R,ref}^{\angle v_s} - \underline{i}_R^{\angle v_s}) \\ &= -\underline{G}_{FFI} \underline{i}_R^{\angle v_s} + \underline{G}_{FFV} \underline{v}_S^{\angle v_s} - \underline{G}_{PI} (\underline{i}_{R,ref}^{\angle v_s} - \underline{i}_R^{\angle v_s}) \end{aligned} \tag{22}$$

The structure of the DFIG inner current control loop is shown in **Figure 12** with the transfer function of $G_{meas}(s)$ and $G_{dt}(s)$ which are the same as for LSC. The closed-loop transfer function of the DFIG stator current then becomes

$$\underline{i}_S^{\angle 0} = \frac{N_1(s) \underline{i}_{R,ref}^{\angle 0} + N_2(s) \underline{v}_S^{\angle 0}}{1 + D(s)} \tag{23}$$

where

$$\begin{aligned} D(s) &= G_{RR}(s) \cdot G_{dt}(s - j\omega_R) \cdot (\underline{G}_{FFI} - G_{PI}(s) \cdot G_{meas}(s - j\omega_R)) \\ N_1(s) &= -G_{SR}(s) \cdot G_{PI}(s) \cdot G_{dt}(s - j\omega_R) \\ N_2(s) &= D(s) \cdot (G_{DVR}(s) - G_{DVS}(s)) + G_{SR}(s) \cdot \\ &\quad G_{dt}(s - j\omega_R) \cdot G_{meas}(s) \cdot \underline{G}_{FFV} + G_{DVS}(s) \end{aligned} \tag{24}$$

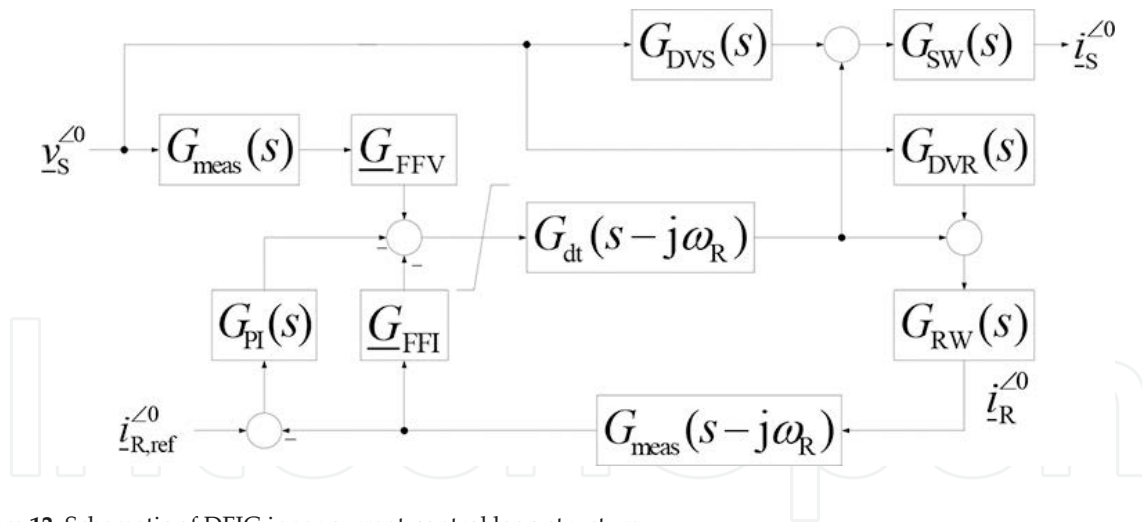


Figure 12. Schematic of DFIG inner current-control loop structure.

The characteristic polynomial in Eq. (23) is of seventh order, which cannot be solved by radicals because the quartic function is highest degree polynomial that can be solved in radicals. Rather iterative methods, for instance, Newton Raphson can be used for finding the roots.

Figure 13 shows the frequency response of the DFIG stator current, from which it can be concluded that there exist two Eigen frequencies that lie around the operating frequency. Additionally, the measurement and dead-time delays do not influence the response except in the high-frequency region and only in the response to the reference tracking quantity.

Consequently, neglecting both $G_{meas}(s)$ and $G_{dt}(s)$ would not result in significant difference in the dynamic response of the DFIG. This is evident in **Figure 14**, which shows the behavior of the stator current with and without considering $G_{meas}(s)$ and $G_{dt}(s)$.

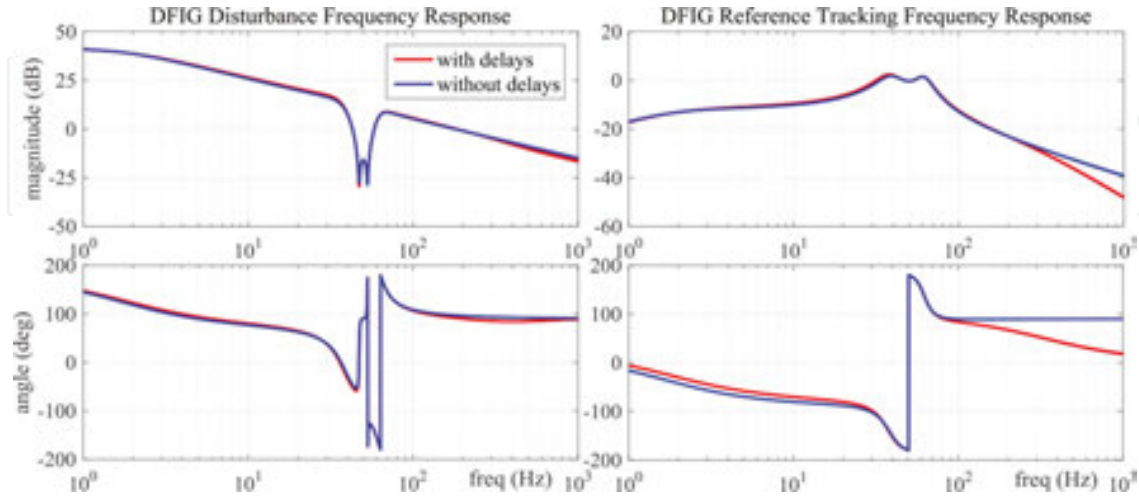


Figure 13. Frequency response of DFIG stator current.

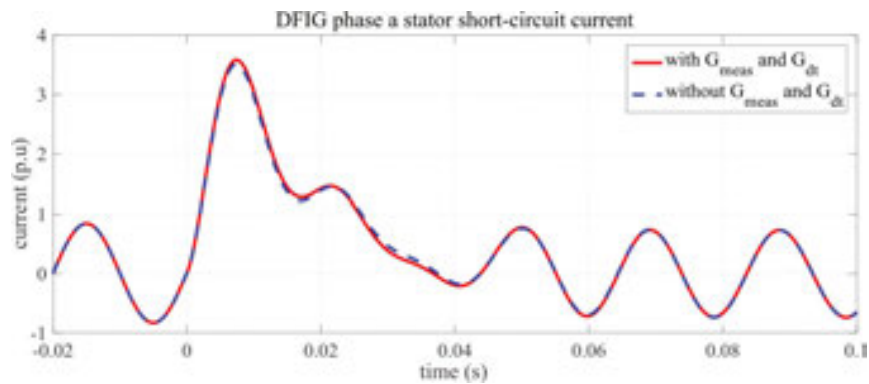


Figure 14. Influence of measurement and dead-time delays on DFIG short-circuit current.

Neglecting $G_{meas}(s)$ and $G_{dt}(s)$ will result in a third order transfer function given by the following:

$$i_s^{<0} = \frac{-((s - j\omega_0)(k_p + l_R(s - j\omega_0)) + k_1)y_s^{<0} - j\omega_0 l_M(k_p(s - j\omega_0) + k_1)i_{Ref}^{<0}}{(k_p(s - j\omega_0) + k_1)(r_s + j\omega_0 l_s) + l_R(s - j\omega_0)(s - j\omega_0)(r_s + j\omega_0 \sigma l_s)} \quad (25)$$

The time constants and Eigen frequencies of Eq. (25) can be found by solving the general cubic formula [13]. However, this would result in complex formulas [18], and an easier way is to again apply singular perturbation as before which would result in more relaxed formulas as follows:

$$\begin{aligned} \frac{1}{\tau_{DC}} - j\omega_{DC} &\approx \frac{r_s (\omega_0^2 l_R - k_I + j\omega_0 k_P)}{l_s (\omega_0^2 \sigma l_R - k_I + j\omega_0 k_P)} \\ \frac{1}{\tau_{AC,12}} - j\omega_{AC,12} &\approx \frac{k_p (r_s + j\omega_0 l_s)}{2l_R (r_s + j\omega_0 \sigma l_s)} - j \left(\omega_0 \pm \sqrt{\frac{k_I (r_s + j\omega_0 l_s)}{l_R (r_s + j\omega_0 \sigma l_s)}} \right) \\ \underline{z}'_s &\approx r_s + j\omega_0 l_s \frac{(\omega_0^2 \sigma l_R - k_I + j\omega_0 k_P)}{(\omega_0^2 l_R - k_I + j\omega_0 k_P)} \end{aligned} \tag{26}$$

Finally, the fault current response of the DFIG with feed-forward control can be expressed as follows:

$$i_{-s}^{\angle 0}(t) \approx i_{-s,ss}^{\angle 0} - \frac{\Delta v_s^{\angle 0}}{\underline{z}'_s} e^{-\left(\frac{1}{\tau_{DC}} - j\omega_{DC}\right)t} + \left(\frac{\Delta v_s^{\angle 0}}{\underline{z}'_s} - \frac{j\omega_0 l_M \Delta i_{Ref}^{\angle 0}}{r_s + j\omega_0 l_s} \right) \left(\frac{e^{-\left(\frac{1}{\tau_{AC1}} - j\omega_{AC1}\right)t} + e^{-\left(\frac{1}{\tau_{AC2}} - j\omega_{AC2}\right)t}}{2} \right) \tag{27}$$

where the steady state current is given by the following:

$$i_{-s,ss}^{\angle 0} = \frac{j\omega_0 l_M \Delta i_{Ref}^{\angle 0} + v_s^{\angle 0}}{r_s + j\omega_0 l_s} \tag{28}$$

The resultant transient short-circuit current components from Eq. (27) in comparison with the transient current from simulation are shown in **Figure 15**.

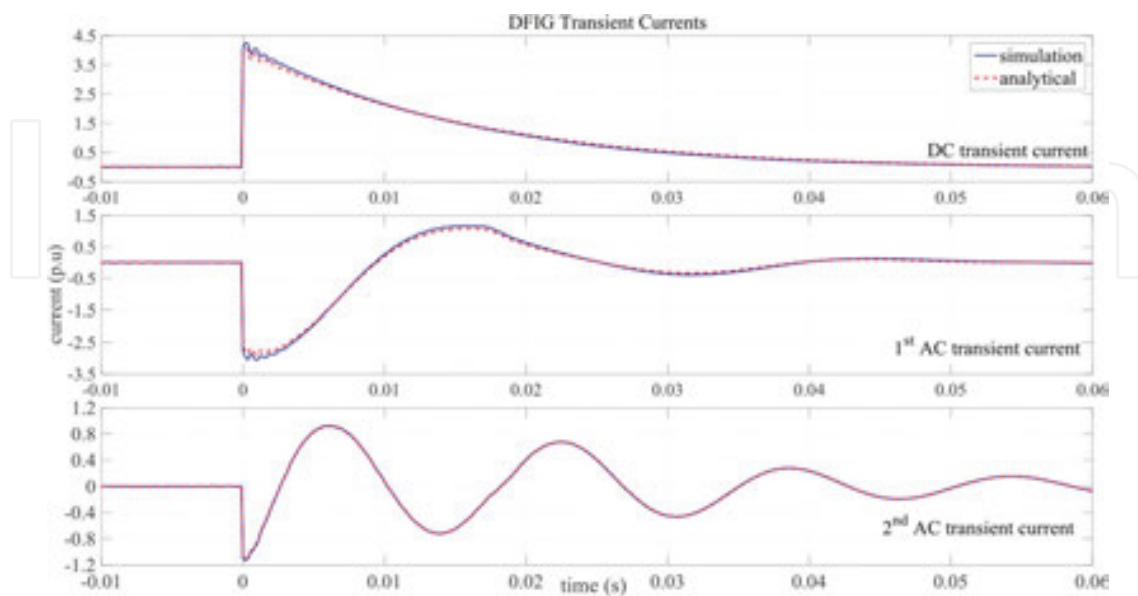


Figure 15. DFIG stator short-circuit current transient components.

4. Standard method for calculation of DFIG-WT fault current contribution

The fault current contribution of the DFIG-WT can be directly calculated through electromagnetic transient (EMT) calculation. However, this would be inconvenient in large network with large number of machines due to the high-computational effort required. Therefore, the calculation methods offered in IEC-60909 are usually used. This is attributed to its simplicity and reliable procedures, which are based on equivalent voltage source calculation and correction factors that offer sufficient accuracy.

The procedures for fault current calculation according to IEC-60909 are as follow:

$$I_k'' = \frac{cU_n}{\sqrt{3}Z''} \quad (29)$$

$$i_p = \sqrt{2}\kappa I_k''$$

where I_k'' is the initial symmetrical short-circuit current, i_p is the peak short-circuit current, c is the voltage correction value, Z'' is the sub-transient impedance, and κ is a term that accounts for the exponential decay of the current and is given by the following:

$$\kappa = 1.02 + 0.98e^{-3R/X} \quad (30)$$

IEC-60909 offers three different methods for R/X ratio calculation in meshed networks, viz.:

Method A: the factor κ is calculated based on Eq. (30) taking the smallest ratio of R/X in all branches.

Method B: The R/X ratio is calculated from the equivalent impedance seen from the short-circuit location. A correction value 1.15 modifies the factor κ to cover inaccuracies caused using R_k/X_k ratio from network reduction with complex impedances.

Method C: The equivalent impedance seen from short-circuits location is calculated assuming $f_c = 20\text{Hz}$, then the R/X ratio is calculated by the following:

$$\frac{R}{X} = \frac{R_c}{X_c} \cdot \frac{f_c}{f} \quad (31)$$

Although IEC-60909 offers a fast and reliable method for fault current calculation, it is not adequate for calculation of fault currents from DFIG-WT; because it assumes a constant transient/internal voltage [19]. However, in DFIG-WT, the controller reacts fast upon fault occurrence and manipulates the internal voltage in order to comply with the grid codes, and consequently influence the short-circuit quantities in accordance with Eqs. (26) and (27).

4.1. Influence of PI-controller on the short-circuit current quantities

According to Eqs. (26) and (27), the PI-controller has a great influence on the behavior of the DFIG stator. In order to validate those expressions and examine their influences, the different transient current components are extracted from the simulated fault current by means of nonlinear optimization which minimizes the objective function:

$$\min_x \sum_i (F(x, xdata_i) - y_i)^2 \quad (32)$$

where y_i is the simulated short-circuit current, and $F(x)$ is the proposed solution, which was considered to be a summation of the four current components proposed in Eq. (27) described by the following:

$$i_s(t) = |i_{s,ss}| \sin(\omega_0 t + \varphi_0) + |i_{DC}| e^{-\frac{t}{\tau_{DC}}} \sin(\omega_{DC} t + \varphi_{DC}) + |i_{AC1}| e^{-\frac{t}{\tau_{AC1}}} \sin(\omega_{AC1} t + \varphi_{AC1}) + |i_{AC2}| e^{-\frac{t}{\tau_{AC2}}} \sin(\omega_{AC2} t + \varphi_{AC2}) \quad (33)$$

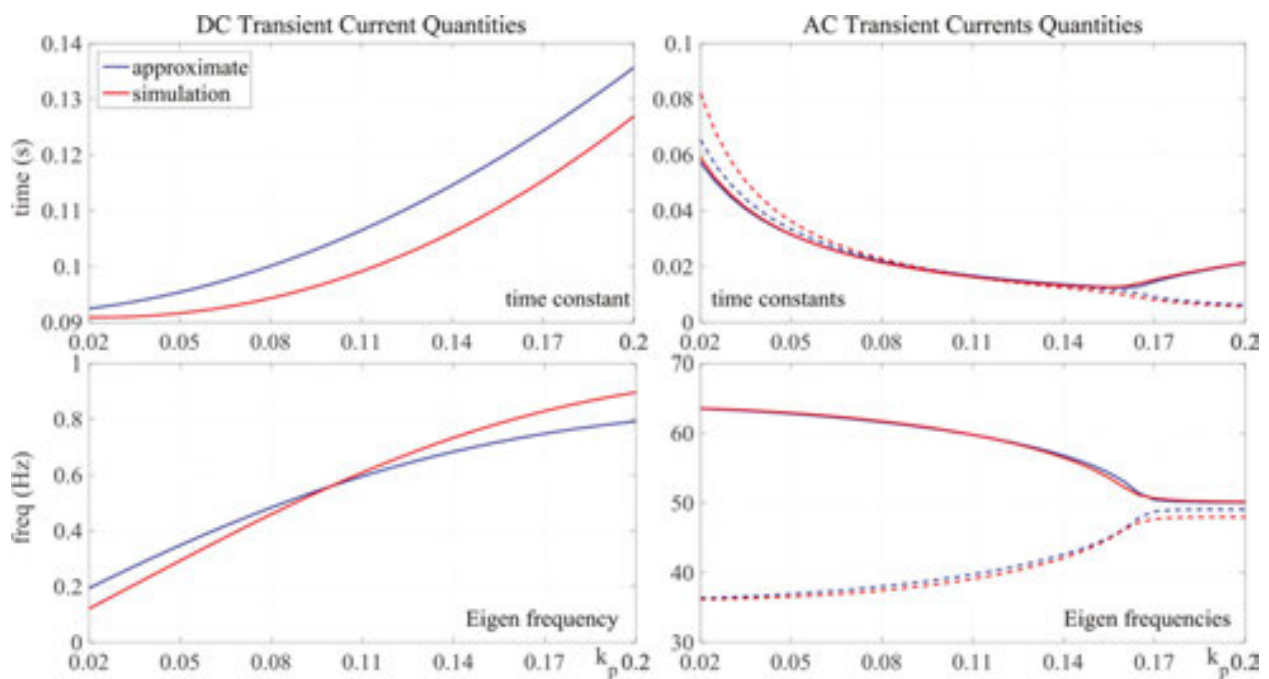


Figure 16. Influence of the proportional gain on time constants and Eigen frequencies.

Figures 16–18 show the influence of the PI-controller on the short-circuit current components, and the following could be concluded:

- the expressions given in Eqs. (26) and (27) tally with the simulation results with small errors;

- the integral gain does not have great influence on the peak values of the short-circuit current because it does not influence the time constants significantly;
- the IEC-60909 method does not consider the controller parameters and therefore does not offer accurate results.

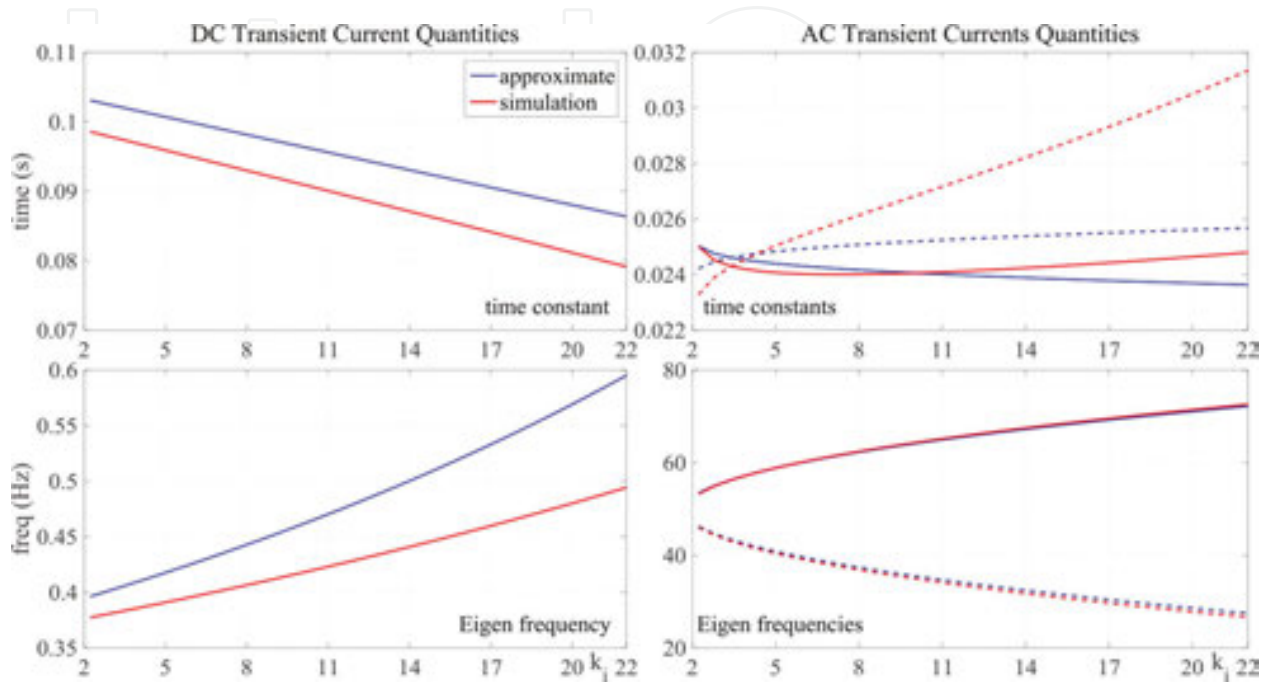


Figure 17. Influence of the integral gain on time constants and Eigen frequencies.

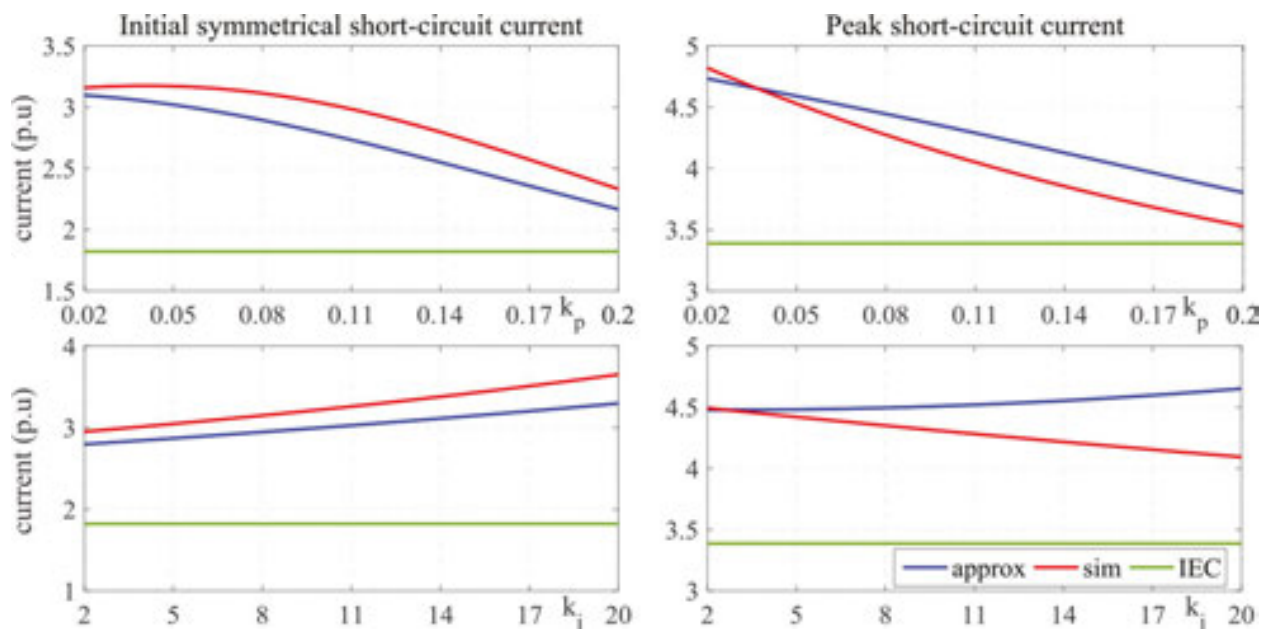


Figure 18. Influence of the PI-controller on short-circuit current values.

4.2. Standard calculation methods

As shown already, the integral gain does not influence the peak current values as well as the time constants. For sake of simplicity, it can be ignored and the Eqs. (26) and (27) can be reduced to the following:

$$\begin{aligned} \frac{1}{\tau_{DC}} - j\omega_{DC} &\approx \frac{r_s(k_p - j\omega_0 l_R)}{l_s(k_p - j\omega_0 \sigma l_R)}, \quad \frac{1}{\tau_{AC}} - j\omega_{AC} \approx \frac{k_p(r_s + j\omega_0 l_s)}{l_R(r_s + j\omega_0 \sigma l_s)} - j\omega_0 \\ \underline{z}'_s &\approx r_s + j\omega_0 l_s \frac{(k_p - j\omega_0 l_R)}{(k_p - j\omega_0 \sigma l_R)} \\ \underline{i}_s^{\angle 0}(t) &\approx \underline{i}_{s,ss}^{\angle 0} - \frac{\Delta v_s^{\angle 0}}{\underline{z}'_s} e^{-\left(\frac{1}{\tau_{DC}} - j\omega_{DC}\right)t} + \left(\frac{\Delta v_s^{\angle 0}}{\underline{z}'_s} - \frac{j\omega_0 l_M \Delta i_{ref}^{\angle 0}}{r_s + j\omega_0 l_s} \right) e^{-\left(\frac{1}{\tau_{AC}} - j\omega_{AC}\right)t} \end{aligned} \quad (34)$$

Expressing the short-circuit current in phasor form yields the following:

$$\begin{aligned} i_s(t) &= |i_{s,ss}| \sin(\omega_0 t - \varphi_0 + \varphi_U) \\ &\quad + |i_{DC}| e^{-\frac{t}{\tau_{DC}}} \sin(\omega_{DC} t + \varphi_{DC} - \varphi_U) \\ &\quad + |i_{AC}| e^{-\frac{t}{\tau_{AC}}} \sin(\omega_{AC} t - \varphi_{AC} + \varphi_U) \end{aligned} \quad (35)$$

Eq. (35) is not similar to the IEC-60909 method for peak value calculation as given in Eq. (29) because the proposed current model contains three components. In order to similarize, the current model to model of IEC-60909 linearization of the proposed current model can be applied.

Ignoring the phase difference in the same manner as IEC-60909 and equating the peak current of Eq. (35) with the one from IEC-60909 in Eq. (29) yields the following:

$$\begin{aligned} |i_{s,ss}| + |i_{AC}| e^{-\frac{t_p}{\tau_{AC}}} + I'_k e^{-\frac{t_p}{\tau_{DC}}} &= I'_k \left(1 + e^{-3\frac{R}{X}} \right) \\ c_{ss} I'_k + (1 + c_{ref}) I'_k e^{-\frac{t_p}{\tau_{AC}}} + I'_k e^{-\frac{t_p}{\tau_{DC}}} &= I'_k \left(1 + e^{-3\frac{R}{X}} \right) \\ c_{ss} + (1 + c_{ref}) e^{-\frac{t_p}{\tau_{AC}}} + e^{-\frac{t_p}{\tau_{DC}}} &= 1 + e^{-3\frac{R}{X}} \end{aligned} \quad (36)$$

where $t_p \approx 0.01s$ is the time instant for the occurrence of the peak, $c_{ss} = |i_{S,ss} + i_{LSC,ss}| / I'_k$ and

$$c_{ref} = - \left| \frac{j\omega_0 l_M \Delta i \angle 0}{r_s + j\omega_0 l_s} + \Delta i \angle 0 \right|_{LSC,Ref} / I'_k .$$

Applying Taylor expansion of the exponential parts and neglecting the higher-order terms yields the equivalent R/X ratio of the DFIG-WT as follows:

$$c_{ss} + c_{ref} \left(1 - \frac{t_p}{\tau_{AC}} \right) - \frac{t_p}{\tau_{AC}} - \frac{t_p}{\tau_{DC}} \approx -3 \frac{R}{X}$$

$$c_{cont} = 0.033 \left(\frac{t_p}{\tau_{AC}} - c_{ss} - c_{ref} \left(1 - \frac{t_p}{\tau_{AC}} \right) \right) \tag{37}$$

$$\frac{R}{X} \approx c_{cont} + \frac{r_s}{\omega_0 \sigma l_s}$$

The correction factor c_{cont} is newly introduced to account for the influential behavior of the controller on the short-circuit current. It can be directly calculated if all controller parameters are known. Otherwise, it can be calculated using measurement. Using of measurement to estimate c_{cont} is preferred as it offers better and more accurate values because not all controller parameters or structures follow what has been introduced here and they vary from manufacturer to manufacturer. Additionally, the measurement would account for the deviation of the transient impedance from the one offered by the manufacturer and to the deviation in the time occurrence of the peak value from the one offered by IEC-60909 and to the error in the linearization process.

4.3. Validation of the calculation method

The test network in **Figure 19** is used to validate the proposed calculation method. A manufacturer provided simulation model of DFIG-WT (real-world parameters are used, so that the results reflect the real dynamic behavior as closely as possible) is implemented and the ratings of the DFIG-WT are found in the Appendix.

The test networks consists of a wind farm that contains 10 DFIG-WTs connected via two winding step-up transformer to 20 kV medium voltage point of common coupling (PCC) designated as K10. The PCC is connected by a medium voltage cable of length 13 kM to the main bus K11, which is connected to the 110 kV high-voltage bus K12 by two windings step-up transformer. Three different short-circuits were applied at K10, K11, and K12, and the values of the short-circuit current using the proposed method and IEC-60909 were calculated and compared to the simulation results **Tables 1–3**.

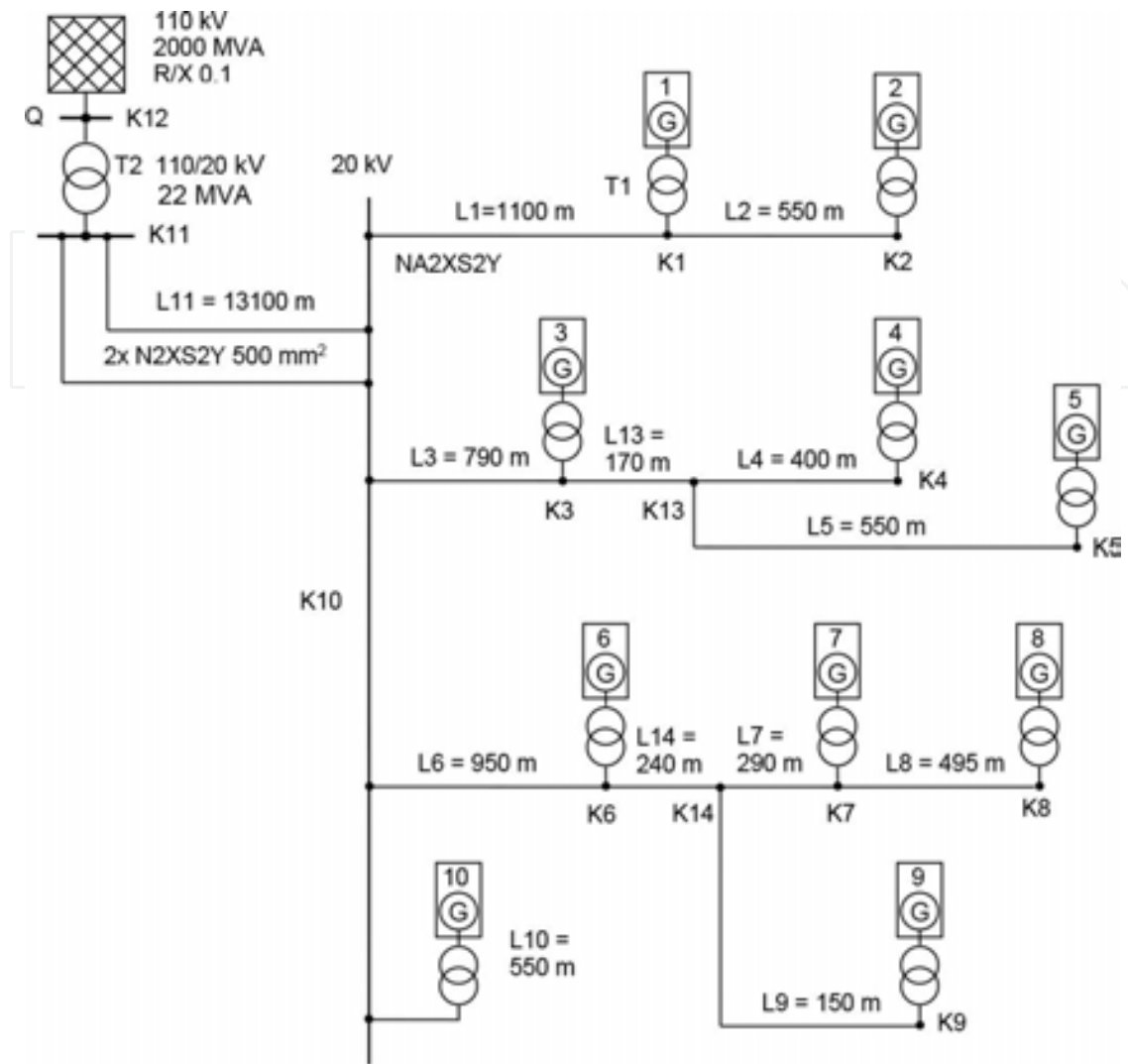


Figure 19. Simulation network.

| R/X | K 10 | K 11 | K 12 |
|------------|-------|------|------|
| IEC-60909 | 0.23 | 0.1 | 0.1 |
| New method | 0.296 | 0.16 | 0.11 |

Table 1. R/X ratio as seen from K 10, K 11, and K 12.

| I'_k (kA) | K 10 | | | | | K 11 | | | | K 12 | | |
|-------------|------|------|------|------|------|------|------|------|------|------|------|-------|
| | L10 | L6 | L3 | L1 | L11 | K10 | L11 | T2 | K11 | T2 | Grid | K12 |
| IEC-60909 | 0.22 | 0.87 | 0.66 | 0.44 | 3.67 | 5.86 | 1.82 | 5.45 | 7.23 | 0.25 | 10.5 | 10.75 |
| New method | 0.26 | 1.01 | 0.77 | 0.51 | 3.7 | 6.2 | 2.06 | 5.45 | 7.5 | 0.28 | 10.5 | 10.78 |

Table 2. Initial symmetrical short-circuit current at K 10, K 11, and K 12.

| i_p (kA) | K 10 | | | | | K 11 | | | | K 12 | | |
|-------------|------|------|-----|------|-----|------|-----|------|------|------|-------|------|
| | L10 | L6 | L3 | L1 | L11 | K10 | L11 | T2 | K11 | T2 | Grid | K12 |
| IEC-60909 C | 0.47 | 1.86 | 1.4 | 0.94 | 7.8 | 12.5 | 4.5 | 13.4 | 17.8 | 0.63 | 25.8 | 26.4 |
| IEC-60909 B | 0.54 | 2.1 | 1.6 | 1.1 | 9 | 14.3 | 5 | 15.1 | 20.0 | 0.72 | 29.7 | 30.4 |
| New method | 0.4 | 1.6 | 1.2 | 0.8 | 8.1 | 11.1 | 3.4 | 14.3 | 16.1 | 0.5 | 25.9 | 26.1 |
| Simulation | 0.4 | 1.6 | 1.2 | 0.79 | 7.1 | 11 | 3.3 | 12.6 | 15.4 | 0.5 | 25.62 | 26 |

Table 3. Peak short-circuit current at K 10, K 11, and K 12.

5. Conclusion

The fault current contribution of DFIG-WTs is dictated by a combination of factors, including the electrical parameters of the machine and the converter controller configuration. A detailed analysis of the DFIG-WT fault response was introduced considering all controller parameters and configurations.

It was shown that ignoring delays introduced by the measurement and PWM converter do not lead to significant difference in the dynamic response of both DFIG and LSC. Additionally, the simplification led to full dynamic rejection of the disturbance quantity in the LSC current response and reduced order model of the DFIG stator current.

The analysis of the fault response of the LSC showed that the dynamics of the LSC current are too fast and of small magnitude and can safely be ignored. Consequently, the LSC fault response can be modeled as a current source with the reference currents as a set-point. On the other hand, the analysis of the fault current response of the DFIG showed that the PI-controller has a great influence on the dynamics of the current. Therefore, approximate expressions were provided for the short-circuit parameters which agree well with the values estimated from simulation.

The simplified and reliable procedures for short-circuit current calculation offered by IEC-60909 is not suitable for DFIG-WT and may lead to overdesign of circuit breakers and bus bars as well as improper setting of protective relays. Therefore, a new standard and simple method for calculation of fault current contribution of DFIG-WT was introduced to overcome the deficiency of the IEC-60909 but with the same procedures. The method was derived by reducing the proposed current model by ignoring the integral gain, which was already shown that it does not influence the time constants and consequently the peak value, then using Taylor expansion of the exponential terms to estimate the equivalent R/X ratio, where a new correction factor named controller factor was introduced. The newly introduced correction factor considers the influencing behavior of the controller and its various configurations and can be estimated based on measurement.

In order to validate the efficiency of the new method, a small wind farm of 10 DFIG-WTs was implemented using a detailed manufacturer-based model. Three-phase short-circuits were

applied at three different places and the results from IEC-60909, and the proposed method were compared to the results from the simulation. The comparison showed that the proposed method offers very accurate results in comparison with IEC-60909 especially when the short-circuit locations were near the DFIG-WTs.

6. Appendix

$$\begin{aligned}
 V_s &= 690\text{V}, V_R = 1.7\text{kV}, r_s = 0.00206\Omega, l_s = 0.0027\text{H} \\
 r_R &= 0.00607\Omega, l_R = 0.0027\text{H}, l_M = 0.0026\text{H}, \text{ Pole Pairs} = 2 \\
 V_{dc} &= 1100\text{V}, c_{dc} = 0.038\text{F chopper on / off} = 1.07 / 1.04V_{dc}
 \end{aligned}
 \tag{38}$$

Author details

Ahmed El-Naggar

Address all correspondence to: ahmed.elnaggar@uni-due.de

Institute of Electrical Power Systems, University of Duisburg-Essen, Duisburg, Germany

References

- [1] H. Polinder, "Overview of and trends in wind turbine generator systems," in *2011 IEEE Power and Energy Society General Meeting*, 2011, pp. 1–8.
- [2] H. Li and Z. Chen, "Overview of different wind generator systems and their comparisons," *IET Renew. Power Gener.*, vol. 2, no. 2, pp. 123–138, 2008.
- [3] F. Blaabjerg and K. Ma, "Future on power electronics for wind turbine systems," *IEEE J. Emerg. Sel. Top. Power Electron.*, vol. 1, no. 3, pp. 139–152, 2013.
- [4] O. Anaya-Lara, N. Jenkins, J. Ekanayake, P. Cartwright, and M. Hughes, *Wind Energy Generation: Modelling and Control*, 1. Auflage. Chichester, U.K: John Wiley & Sons, 2009.
- [5] M. Z. B. Sujod, "Advanced converter control techniques for improving the performances of DFIG based wind turbines," Ph. D Dissertation, Electrical Power System, Duisburg-Essen, Duisburg, Germany, 2014.
- [6] N. Mohan, T. M. Undeland, and W. P. Robbins, *Power Electronics: Converters, Applications, and Design*, 3. Auflage. Hoboken, NJ: John Wiley & Sons, 2002.

- [7] A. Wintrich, U. Nicolai, W. Tursky, and T. Reiman, *Application Manual Power Semiconductors*, 2nd ed. Nuremberg, Germany: SEMIKRON International GmbH, 2015.
- [8] *The Induction Machines Design Handbook*, 2nd ed. Boca Raton, FL: CRC Press, 2009.
- [9] E. Muljadi, N. Samaan, V. Gevorgian, J. Li, and S. Pasupulati, "Short circuit current contribution for different wind turbine generator types," in *2010 IEEE Power and Energy Society General Meeting*, 2010, pp. 1–8.
- [10] P. Karaliolios, A. Ishchenko, E. Coster, J. Myrzik, and W. Kling, "Overview of short-circuit contribution of various Distributed Generators on the distribution network," in *Universities Power Engineering Conference, 2008. UPEC 2008. 43rd International*, 2008, pp. 1–6.
- [11] J. Morren and S. W. H. de Haan, "Short-circuit current of wind turbines with doubly fed induction generator," *IEEE Trans. Energy Convers.*, vol. 22, no. 1, pp. 174–180, 2007.
- [12] G. Pannell, D. J. Atkinson, and B. Zahawi, "Analytical study of grid-fault response of wind turbine doubly fed induction generator," *IEEE Trans. Energy Convers.*, vol. 25, no. 4, pp. 1081–1091, 2010.
- [13] C. Feltes, "Advanced Fault Ride Through Control of DFIG Based Wind Turbines Including Grid Connection Via VSC-HVDC," Ph. D Dissertation, Electrical Power System, Duisburg-Essen, Duisburg, Germany, 2012.
- [14] F. Klein, *Lectures on the Icosahedron and the Solution of Equations of the Fifth Degree*. London: Trübner & Co., 1888.
- [15] D. S. Dummit, "Solving solvable quintics," *Math. Comput.*, vol. 57, no. 195, pp. 387–401, 1991.
- [16] V. S. Adamchik and D. J. Jeffrey, "Polynomial transformations of tschirnhaus, bring and jerrard," *SIGSAM Bull.*, vol. 37, no. 3, pp. 90–94, 2003.
- [17] W. H. Press, B. P. Flannery, S. A. Teukolsky, and W. T. Vetterling, *Numerical Recipes in FORTRAN 77: Volume 1, Volume 1 of Fortran Numerical Recipes: The Art of Scientific Computing*, 2nd ed. Cambridge England; New York: Cambridge University Press, 1992.
- [18] A. El-Naggar and I. Erlich, "Analysis of fault current contribution of Doubly-Fed Induction Generator Wind Turbines during unbalanced grid faults," *Renew. Energy*, vol. 91, pp. 137–146, 2016.
- [19] A. El-Naggar, C. Feltes, and I. Erlich, "R/X ratio influence on short circuit current of doubly-fed induction generator based wind turbines," in *2013 IEEE Power and Energy Society General Meeting (PES)*, 2013, pp. 1–5.

